Journal Pre-proof

High thermal conductivity of boron nitride filled epoxy composites prepared by tin solder nanoparticle decoration

Eun-Sung Lee, Jong-Gu Kang, Min-Kyeong Kang, Ki-Hong Kim, Seon-Tae Park, Yong Su Kim, In Kim, Sung-Dug Kim, Jin-Young Bae

PII: S1359-8368(21)00640-5

DOI: https://doi.org/10.1016/j.compositesb.2021.109264

Reference: JCOMB 109264

To appear in: *Composites Part B*

Received Date: 3 June 2021

Revised Date: 26 August 2021

Accepted Date: 27 August 2021

Please cite this article as: Lee E-S, Kang J-G, Kang M-K, Kim K-H, Park S-T, Kim YS, Kim I, Kim S-D, Bae J-Y, High thermal conductivity of boron nitride filled epoxy composites prepared by tin solder nanoparticle decoration, *Composites Part B* (2021), doi: https://doi.org/10.1016/j.compositesb.2021.109264.

CRediT authorship contribution statement

Lee E-S: Conceptualization and Data curation, Investigation, Formal analysis, Writing original draft, Writing - review & editing, Supervision. **Kang J-G & Kang M-K:** Investigation, Formal analysis. **Kim K-H:** Formal analysis. **Park S-T:** Formal analysis. **Kim Y-S:** Formal analysis. **Kim I:** Project administration. **Kim S-D:** Project administration. **Bae J-Y:** Writing original draft, Writing - review & editing.

Data availability Statement

The datasets generated and/or analyzed during this study can be made available from the corresponding author on reasonable request.

High Thermal Conductivity of Boron Nitride Filled Epoxy Composites Prepared by Tin Solder Nanoparticle Decoration

Eun-Sung Lee[a], Jong-Gu Kang[b], Min-Kyeong Kang[b], Ki-Hong Kim[a], Seon-Tae Park[a], Yong Su Kim[a], In Kim[a], Sung-Dug Kim[a], and Jin-Young Bae[a**]*

[a] Material Research Center, Samsung Advanced Institute of Technology, Samsung Electronics Co., Ltd., Suwon, 16678, Republic of Korea

[b] Department of Polymer Science and Engineering, Sungkyunkwan University, Suwon, 440-746, Republic of Korea

* Corresponding author.

** Corresponding author.

E-mail addresses: esleeone@gmail.com (E.-S. Lee); b521@skku.edu (J.-Y. Bae)

Keywords: Thermal conductivity, Epoxy composites, Hexagonal boron nitride, Tin nanoparticle decoration, Tin nanoparticle in situ growth

To achieve a high thermal conductivity, thermally conductive polymer composites have been recently exploited, focusing on connecting a 3D network of thermally conductive fillers by applying external pressure or constructing a pre-made 3D filler framework to reduce phonon scattering within the polymer matrix. However, these approaches severely restrict the use of polymers, particularly epoxy composites, in many commercial applications such as the thermal management of electronic device packaging. In this study, a high-thermal-conductivity epoxy composite is fabricated by incorporating hexagonal boron nitride (*h*-BN) decorated with tin nanoparticles (Sn NPs). Under a hybrid filler (Sn NPs on *h*-BN) loading (68 wt. %), the composite exhibits a high thermal conductivity of 11.9 ± 0.29 W m^{-1} K^{-1} while maintaining a

relatively low dielectric constant (D_k ~ 7.52) and loss (D_f ~ 0.023) at 1 MHz with a coefficient of thermal expansion of 34 ppm $°C^{-1}$. The Sn NPs on *h*-BN in the epoxy resin matrix are thermally percolated by the in-situ growth of Sn NPs under carefully controlled curing temperature and time, resulting in significantly improved thermal conductivity of the epoxy composite under pressure-less curing conditions.

1. Introduction

Thermally conductive filler-based epoxy composites have been extensively studied for semiconductor packaging applications. These composites can be prepared with epoxy molding compound (EMC), under-filling substances, thermal interface materials (TIMs), and glob tops [1–4,]. In the last few decades, multi-stacked chips and small package sizes have been trending, driven by the need for portable consumer products and lower manufacturing costs. In addition, the device speeds have continued to increase, leading to the generation of more heat within a smaller chip volume. These factors limit the high power dissipation or high "clock" frequency of semiconductor chips because of the low thermal conductivity of presently available epoxy resin-based composites. Unfortunately, a cured epoxy resin has poor thermal properties such as a high coefficient of thermal expansion (CTE) and low thermal conductivity [5].

The incorporation of high-thermal-conductivity fillers into an epoxy resin is the most effective way to enhance the thermal conductivity of epoxy resin-based composites. The fillers require only phonon conduction with electrical insulation; examples of fillers include diamond, beryllium oxide (BeO), aluminum nitride (AlN), aluminum oxide (Al_2O_3), and boron nitride (BN), the crystalline structure of which can be hexagonal (*h*-BN) or cubic (c-BN) [5,6]. Diamond and c-BN are ideal fillers for heat conduction; however, they are expensive, and beryllium oxide is toxic. The theoretical thermal conductivity of Al_2O_3 is approximately in the range of 38~42 W m^{-1} K^{-1}, which is lower than those of AlN and *h*-BN. Hexagonal boron

nitride (*h*-BN), including some of its nanoscale moieties, namely BN nanosheet (BNNS), BN nanoplatelet (BNNP), and BN nanotube (BNNT), has a high thermal conductivity, reasonably low CTE, and low dielectric constant [7, 8]. Many researchers have conducted studies on improving the thermal conductivity of epoxy polymer composites by adding high-thermal-conductivity solid fillers such as *h*-BN, BNNS or graphene [9–15]. Many factors affect the thermal conductivity of composite materials, including the intrinsic thermal conductivity of the fillers, the filler dispersion state in the matrix, the interfacial interaction between the filler and matrix, and the orientation degree of the fillers in the matrix [16–18]. Among these factors, the inter-filler contact and the filler alignment in the polymer matrix play the most important roles in improving the thermal conductivity of polymer composites, given the inevitable phonon scattering at the filler–polymer interface; moreover, the interfacial thermal resistance deteriorates the thermal conductivity [19–21].

In the last few years, research has focused on connecting a 3D network of thermally conductive fillers to reduce phonon scattering within the polymer matrix [22–24]. Several methods have been implemented, including surface modification with organic molecules or silver nanoparticles (Ag NPs) [25–27], external pressure application, and freeze-casting or use of aerogels followed by polymer infiltration [22,24]. Liu et al. [28] spin-coated and hot-pressed BNNS treated with aminopropyl triethoxysilane (APTES) at 5 MPa. The thermal conductivity was found to be 5.86 W m^{-1} K^{-1} under a BNNS loading of 40 wt.% (25 vol.%), with improved BNNS in-plane orientation. The formation of covalent bonds on the BNNS surface improved the filler–epoxy interface contact and resulted in a high thermal conductivity under a small amount of BNNS loading. Chen et al. [29] fabricated a multilayer epoxy composite composed of BNNS and AlN platelets under a 10 MPa hot-pressing condition. They realized a high thermal conductivity of 8.53 W m^{-1} K^{-1} owing to the improvement in the inter-filler contact and alignment by applying a relatively high pressure and optimizing the filler particle shape. Xiao et al. reported a maximum thermal conductivity of 17.61 W m^{-1} K^{-1} (in-plane direction)

and 5.08 W m^{-1} K^{-1} (out-of-plane direction) at a BNNP loading of 65.6 vol. % [30]. They fabricated a thermally conductive composite by synthesizing boron nitride microbead (BNMB) hollow spheres and applying a compressive force followed by infiltrating the epoxy resin. The high thermal conductivity could be attributed to the high surface area of BNNP, leading to better filler contact area with the bead shape of BN, while reducing the friction during compression. These factors make it possible to achieve a high filler loading for epoxy resin and high thermal conductivity of the composites. Zhang et al. [31] introduced Ag NPs on *h*-BN surfaces by wet-impregnation methods and aligned the orientation of Ag NPs on *h*-BN fillers by hot pressing under 0.2 MPa, representing an effective approach to improve the thermal conductivity. With their method, owing to the improved contact facilitating the heat flow at the interface by the Ag NPs and maximized overlapping area of *h*-BN by hot-pressing, the in-plane ($\lambda_{\parallel}$) and out-of-plane ($\lambda_{\perp}$) thermal conductivity values were reported to be 23.1 and 3.6 W m^{-1} K^{-1}, respectively, under a 60 vol.% loading of Ag NPs on *h*-BN. Thus far, this has been the best thermal conductivity value reported for electrically insulated filler-based epoxy systems. Although the deposition of Ag nanoparticles on the filler surface plays an important role, it is difficult to achieve a high thermal conductivity for epoxy composites without applying an external pressure for filler orientation and alignment. Chen et al. [32] constructed a 3D BNNS network, where the fillers were treated with $AgNO_3$ and a reducing agent, followed by in situ curing without applying any pressure. They reported a very low thermal conductivity of 1.13 W m^{-1} K^{-1}, suggesting that an effective 3D filler network cannot be formed without applying external forces. However, applying an external pressure or constructing a pre-made 3D filler framework severely restricts the commercial application of such composites in the electronic device packaging industry. Therefore, it is important to realize a high thermal conductivity for epoxy composites under pressure-less curing conditions.

The objective of this study was to synthesize low-melting-temperature (thus thermo-controllable at general epoxy curing temperatures under 250 ℃) tin nanoparticles (Sn NPs) on

h-BN surfaces by wet-impregnation methods followed by chemical reduction and to fabricate high-thermal-conductivity epoxy composites, while maintaining relatively low dielectric property values and coefficient of thermal expansion (CTE). With the introduction of hybrid fillers, i.e., Sn NPs on *h*-BN, into the epoxy resin matrix, the generation of a thermal conduction path via the action of tin fusion could effectively reduce the thermal contact resistance at the filler–epoxy matrix interface during in situ curing. Consequently, the thermal conductivity of the epoxy composite is significantly improved without having to apply an external pressure. The *h*-BN-decorated Sn-NP-filled epoxy composite proposed in this paper can broaden the application scope of electronic device packaging and has great potential for the thermal management industry.

2. Experimental Section

2.1. Materials

The epoxy monomer ECC (3,4-Epoxycyclohexylmethyl-3',4'-epoxycyclohexane carboxylate), HHPA (hexahydrophthalic anhydride) as a curing agent, and 2-EMIP(2-Ethyl-4-methyl-1H-imidazole-1-propanenitrile) as a catalyst were purchased from Sigma-Aldrich. The solvents, namely DMF (N, N-dimethylformamide) and NMP (N-Methyl-2-pyrrolidone), purchased from Sigma-Aldrich, were used without further purification. PVP (Polyvinyl-pyrrolidone, M.W. ~40 k), silver nitrate ($AgNO_3$), Tin (IV) chloride pentahydrate ($SnCl_4{\cdot}5H_2O$), and sodium borohydride ($NaBH_4$) were also obtained from Sigma-Aldrich. To ensure the mechanical strength of the cured composite at high filler loading, a silane coupling agent, namely GLYMO (3-glycidoxypropyl trimethoxy silane), was purchased from Sigma-Aldrich. The *h*-BN powders (D_{50}: ~15.61 μm, surface area: 2~5 m^2/g) were purchased from Shandong Pengcheng Advanced Ceramic Co., Ltd., (China).

2.2. Synthesis of metal NPs on h-BN surfaces

To stabilize Ag nanoparticles in DMF, *h*-BN with the addition of PVP was prepared by dissolving PVP (10 g) and *h*-BN powder (20 g) in DMF (500 mL). The slurry mixture was sonicated for 60 min and gradually stirred for 12 h followed by filtering and washing thrice with pure ethanol solvents. The filtered cake was vacuum dried at 100 ℃ for 12 h. After mixing of the PVP coating on the *h*-BN powder (0.9 g) in DMF (80 mL) and performing sonication for 60 min, $AgNO_3$ (0.9 g) in aqueous solution (20 mL) was added to this mixed solution, reacted for 12 h up to six days (144 h), and then filtered and washed thrice with DI water. The formation of Ag NPs was confirmed by XRD and SEM. After completely dissolving the precursor $SnCl_4{\cdot}5H_2O$ in NMP and ethanol-mixed solvents (80 mL) based on various weight ratios (*h*-BN: $SnCl_4{\cdot}5H_2O$ = 1:0.5, 1:1, 1:1.5, 1:2, 1:2.5), PVP coating on *h*-BN powder (0.9 g) was added to the solution and sonicated for 60 min. To provide sufficient time for the adsorption of Sn^{4+} ions on the *h*-BN surfaces, the mixed solution was gradually stirred for 24 h. The reducing agent solution, $NaBH_4$ (sodium borohydride) dissolved in NMP, was placed in a syringe pumping system (purchased from *New Era Pump system Inc.*) and injected into the stirring *h*-BN and $SnCl_4{\cdot}5H_2O$ solution at a rate of 1.0 mL/min. The amount of reduction agent was three times that of the Sn precursor in terms of the molar ratio. The Sn NPs were completely synthesized on the *h*-BN surfaces for a 3 h reaction after finishing the injection. The by-products (NaCl and boric acid) and residual anions or cations were removed by sequentially washing thrice with DI water and ethanol during vacuum filtering. After filtering and washing, the obtained powder was dried at 100 ℃ for 6 h in a vacuum oven, and the synthesized Sn NPs were analyzed by XRD and SEM.

2.3. Fabrication of epoxy composites

The epoxy composites with various amounts of hybrid filler-loaded compositions were prepared by the following procedure: (i) wetting and dispersing Ag NPs or Sn NPs on *h*-BN

fillers (w/ or w/o GLYMO) in an ethyl acetate solvent using a high-speed homogenizer mixer for 1 h, (ii) adding a specific amount of epoxy resin and hardener into the solution and mixing (and/or sonicating) the solution for an additional 30 min to obtain a well dispersed solution, (iii) eliminating ethyl acetate solvent in a gradually rotating evaporator for 2 h and degassing the mixture in a vacuum line at room temperature for 30 min, (iv) pouring the corresponding paste into a mold and completely removing the residual solvent under vacuum at 60 °C, (v) curing the pastes in a three-step process at 150 °C, 180 °C, and ≥ 200 °C for 30 min at each temperature.

2.4. Characterizations and Measurements

The X-ray diffraction (XRD) patterns of the metal nanoparticles on *h*-BN surfaces were collected using an X-ray diffractometer (Bruker, d8 Advance) with Cu Kα irradiation at 40 keV and 40 mA. Regarding the experimental conditions, a continuous theta (θ)-2θ scan mode was used with a 2θ range of 20 ~ 70° and a step size of 0.02 for each data point; the LYNXEYE XE detector was used. X-ray photoelectron spectroscopy (XPS) measurements were also carried out, and the core-level structure was measured by a PHI Quantera-II instrument using Al-Kα radiation as the excitation source (1486.6 eV, monochromatic beam with a diameter of 200 μm). To examine the surface and bulk regions, the samples were sputtered with an Ar-ion beam for 0, 0.5, 1.5, 2.5, and 4 min at an acceleration voltage of 1 kV (area of 1×1 mm^2). The atomic concentration was obtained after Shirley background subtraction. To characterize the shape and size of the metal nanoparticles, we carried out scanning electron microscopy (SEM) using SU-9000 (Hitachi) and energy dispersive spectroscopy (EDS) attached on the SEM. The particle size and total area within Sn NPs on *h*-BN were analyzed using image-pro® plus software for automatic counting and measurement. The typical accelerating voltages were 30 kV and 2 kV, and the applied currents were 15 μA and 5 μA, respectively. The transmission electron microscopy (TEM) images were acquired with Titan G2 (FEI) at an accelerating voltage of 200

kV to scrutinize the interface between the metal nanoparticles and *h*-BN in an epoxy matrix. The thermal conductivity (λ) was calculated using the equation $\lambda = \alpha \times Cp \times \rho$. The thermal diffusivity (α) of the samples was determined using a laser flash thermal analyzer (LFA 467, NETZSCH) with a sample 25 mm in diameter and approximately 1 mm in thickness. The samples were spray coated with graphite powder to optimize the absorption of the light flashes. The specific heat capacity (*Cp*) of the samples was measured by differential scanning calorimetry (LFA 467, NETZSCH) operated at a heating rate of 10 °C min^{-1}. The bulk density (ρ) of the samples was obtained using the water displacement method. The thermal diffusivity, specific heat capacity, and density of the samples were characterized at 25°C. For the dielectric measurement, top Au dots (100 nm thick) of 1 mm radius were deposited on the composites using an e-beam evaporator. The dielectric properties of the epoxy composites were measured at frequencies ranging from 1 kHz to 1 MHz with an AC oscillating voltage of 300 mV using an impedance analyzer (HP 4194). The dielectric constant was determined by averaging the values obtained from more than ten measurements performed on different dots. The coefficient of linear thermal expansion was obtained using a thermomechanical analyzer (TMA 6100, SEICO INST.) operating from 25 °C to 240 °C at a heating rate of 5 °C min^{-1} under N_2 purging.

3. Results and Discussion

3. 1. Synthesis of Metal NPs on h-BN Surfaces

Fig. 1 shows the results of synthesized Ag NPs on *h*-BN following a 144-h reaction, in which the SEM images show Ag NP morphologies and EDAX analyses of each element. The particle size distribution of the Ag NPs could be roughly estimated from a few tens of nanometers to the submicron range with an irregular shape. In Fig. 1g, the XRD peaks at 2θ values of 38.2°, 44.3°, and 64.5° can be assigned to the (111), (200), and (220) crystallographic planes of face-centered cubic (fcc) silver crystals, respectively [33,34]. The formation mechanism of Ag NPs

on the *h*-BN surfaces was studied by XPS analysis, identifying Ag^0 states in Ag NPs from Ag^+-ion adsorption on *h*-BN surfaces followed by a reduction reaction in the DMF solution [26,35]. The dissolved $AgNO_3$ precursors dissociated into Ag^+ ions in a polar DMF solution, and the Ag^+ ions are strongly attached onto the *h*-BN surfaces by Coulomb forces. Because the DMF acts as a solvent and as a good reducing agent for Ag^+ ions, a reduction reaction occurs on the *h*-BN surface with the DMF solvent as follows [36]:

$$\mathbf{HCONMe_2 + 2Ag^+ + H_2O \rightarrow 2Ag^0 + Me_2NCOOH + 2H^+} \quad (1)$$

Ag^+ ions have such a low reduction potential (E_0 = 0.83 eV) that they could be easily reduced with a mild reducing agent such as DMF. Therefore, the main drawback of Ag chemical reduction with DMF is the long reaction time, of up to over one week, to obtain a sufficient amount of Ag NPs. The characteristic peak for Ag (111) hardly appears after 48 h of reaction and keeps increasing until 144 h, as shown in Fig. 1g.

Fig. 2 shows the solvent effects of Sn NP synthesis on *h*-BN. The size distribution of Sn NPs is relatively uniform in the case of NMP-rich media, and their sizes are much smaller than those employing EtOH-rich mixed solvents. When increasing the EtOH proportion in the NMP and EtOH co-solvent ratios, severe particle agglomeration, in which the particle size is >300 nm, can be observed on the *h*-BN surfaces, as shown in Fig. 2 a-e. The reduction reaction of $SnCl_4$ to Sn NPs is as follows [37,38]:

$$\mathbf{SnCl_4 + 4NaBH_4 + 4H_2O \rightarrow Sn + 4B(OH)_3 + 4NaCl + 14H_2} \quad (2)$$

In the reduction process, a solvent is essential in an $NaBH_4$-mediated reduction reaction to stabilize the hydride anion (H^-) and any reactive species during the entire reaction sequence [39]. This stabilization is highly dependent on the polarity of the solvent used [40]. A general

trend is apparent with regard to the solvent properties under these reducing conditions. The hydride (H^-) generated from the dissolution of $NaBH_4$ can be used for reducing $SnCl_4$ in both dipolar aprotic solvents, such as DMF and NMP, and polar protic solvents such as EtOH and H_2O. Increased yields, relative to protic solvents, have been obtained in the case of using the dipolar aprotic solvents [41]. In this study, NMP was found to be the best solvent in terms of the rate and selectivity of Sn generation on the *h*-BN surfaces under these reaction conditions, i.e., fairly large amounts of solvent. Yields were reduced when ethanol was added. During the reduction reaction, one of the roles of NMP is to completely dissolve $NaBH_4$, thus generating (and stabilizing) the hydride anion species [41]. The other role in terms of its dipolar characteristics is to function as a bridging molecule (or ligating species or ligand) between H^- and Sn^{4+} in the electron transfer process. Under typical reaction conditions, employing NMP as a solvent in the absence of an additional co-solvent, the reduction reaction proceeded smoothly, but not so efficiently. Further studies using NMP as a solvent in combination with EtOH as a co-solvent were performed. The addition of EtOH (less than or equal to 0–30 wt. %) to the reaction substantially enhanced the reactivity of the hydride (H^-), resulting in a higher reducing rate. It is speculated that the addition of a relatively small amount of EtOH to the reaction slightly decreases the stability of the hydride species, thus increasing the reactivity. However, when the amount of ethanol increases in mixed solvents, the solvation (and stabilization) of the hydride species is much less favored, resulting in vigorous reduction. On the other hand, a EtOH-rich solvent did not produce any better results, probably because of the poor solubility (and less dissociating characteristics) of $NaBH_4$ [42]. In protic solvents, such as EtOH and water, a premature hydride decomposition with the evolution of H_2 gas has been observed, which impedes the reduction reaction significantly. Notably, straight NMP solvent produces rod-like particle growth with particle length of over 100–200 nm, which is not observed in the NMP/EtOH co-solvent system. Moreover, the peak intensity of (200) to (101) in the X-ray spectra of the 100% NMP solvent is asymmetric, and such features imply the formation of rod-

like nanocrystals with a preferred growth orientation. This topic unfortunately falls outside the scope of our research; further investigation is required in this regard. The synthesized Sn NPs with increasing amounts of $SnCl_4 \cdot 5H_2O$ are shown in Fig. S1 under a 100% NMP solvent system. The particle size distribution is in the range of 100–200 nm, and the amount of Sn NPs increases up to the composition of 1: 2.5 (h-BN vs $SnCl_4$) in weight (Fig. S1e). The XRD patterns also help verify rod-like Sn NP formation from the peak intensity ratio of I_{200}/I_{101} in Fig. S2. The survey scans of *h*-BN and Sn NPs on *h*-BN, presented in Fig. 3c, show the presence of Sn, B, N, O, C, and Cl (no other contaminant elements were detected). To investigate the chemical state of the surface and bulk regions, samples were sputtered with an Ar-ion beam for 0, 0.5, 1.5, 2.5, and 4 min at an acceleration voltage of 1 kV (area of 1×1 mm^2). At the surface, shown in Fig. 3d, the Sn NPs mainly comprised tin-metal, tin-oxide, and tin-chloride. As the sputtering progresses, a tin-metal peak gradually increases and becomes exposed to the surface. As-synthesized Sn NPs can be expected to be covered with tin-oxide. This oxide layer could be grown during the H_2O washing process to remove by-products, such as sodium chloride (NaCl) and boric acid (H_3BO_3), as expressed in Equation (2), and could delay the sintering time of Sn NPs during the epoxy curing process.

3.2. Thermal Conductivity and Microstructure of Epoxy Nanocomposites

The epoxy composite with 40 wt. % loading of Sn NPs on *h*-BN filled in ECC/HHPA (1:1 stoichiometry) was characterized by DSC to evaluate the potential role of the Sn NPs in this epoxy system (Fig. S3). The sample exhibited a broad exothermic peak in the range of 70–180 °C, which could be attributed to the reaction between the anhydride groups of the hardener and the epoxy groups of ECC. The subsequent melting transition of Sn NPs is indicated by the maximum endothermic peak at 231 °C. The presence of 40 phr (part per hundreds) Sn NPs on *h*-BN in the ECC/HHPA curing system did not affect the peak curing temperature. However, its presence implies that Sn NPs are randomly dispersed in the epoxy network up to a temperature

of 200 °C, and further heat treatment (higher than 200 °C) can vary the microstructure of the epoxy nanocomposites through the endothermic interactions of Sn NPs.

Three different conductive fillers (*h*-BN, Ag NPs on *h*-BN, and Sn NPs on *h*-BN) were used in the experiment to improve the thermal properties of ECC cured with HHPA. The thermal conductivities of the composites were investigated as a function of the filler loading (≤ 60 wt. %) at 200 ℃ curing for 30 min, as shown in Fig. 4a. Below 40 wt. % filler loading, the thermal conductivities increased linearly with the addition of *h*-BN or hybrid fillers, indicating relatively low thermal conductivity values, under 3 W m^{-1} K^{-1}. It might be reasonably postulated that all the three types of fillers were randomly distributed and did not thermally percolate each other yet. In the region between 40 and 50 wt. % loading, the thermal conductivity rapidly increased with different slopes between the hybrid fillers (Ag NPs or Sn NPs on *h*-BN) and pure *h*-BN-loaded epoxy composites. The conductivity slopes of the hybrid filler composites were steeper than that of the *h*-BN composite, suggesting that metal NPs on *h*-BN take advantage of the connecting phonon conductive path in the epoxy resin matrix. Although the thermal conductivity improved up to 6.625 W m^{-1} K^{-1} at 65 wt. % loading of Sn NP on *h*-BN composite, it is likely that the thermal percolated network was not completely formed and that the phonon scattering still occurred at the interface between the epoxy resin and the conductive fillers. Fig. 4b-c shows the thermal conductivity of the epoxy composites under different curing temperature and time. The thermal conductivity of Sn NPs on the *h*-BN-filled composite was rather sensitive to the curing temperature (Fig. 4b): the increment in the thermal conductivity is over 2 W m^{-1} K^{-1} with only a 60 ℃ rise in the curing temperature, regardless of the filler loading (50 wt.% or 65 wt.%). The curing time was optimized for 60 min at a curing temperature of 240 ℃ with the 65 wt. % filled epoxy composites (Fig. 4c). Under these optimized curing conditions (240 ℃, 60 min), the high filler loading was attempted to further improve the thermal conductivity of Sn NPs on *h*-BN-filled epoxy composites (Fig. 4d), showing that the thermal conductivity sharply increased by 2.7 W m^{-1} K^{-1} only with 3 wt.%

hybrid filler addition. The highest thermal conductivity was achieved, 11.9 W m^{-1} K^{-1}, at 68 wt. % loading without any external force, which is mainly attributed not to the density or specific heat (Fig. 4d, S4) but to the improvement in the thermal diffusivity from the conductive 3D network of the epoxy composite by the in-situ growth of low-melting-point Sn NPs during the curing process. Clearly, there are two inflection points, i.e., the first percolation region at 40 to 50 wt. % and a second percolation region at high Sn NP on *h*-BN filler loading (≥ 65 wt. %); the thermal conductivity is much more sensitive to the region of high filler loading than to the region of low solid loading. This rapid increase in the thermal conductivity carefully controlled by the curing time and temperature can be explained by the sintering process of the Sn NPs. In the solid-state sintering models, the molecules are transported from a high chemical potential region to a low region via several diffusion routes, such as evaporation-condensation, surface-diffusion, grain boundary diffusion, and lattice diffusion, driven by the reduction in the interface or surface energy [43]. Based on the particle's neck growth and surface diffusion [44,45], which has a low activation energy for diffusion path [46], the analytical solution of surface diffusion model was expressed.

$$\left(\frac{X}{R}\right)^5 = \left(\frac{56\delta D_s \Omega \gamma_{sv}}{kTR^4}\right) t \qquad (3)$$

where R is the particle diameter, X is the neck width, t is the sintering time, δ is the effective thickness, Ω is the atomic volume, D_s is the surface diffusivity, γ_{sv} is the surface energy, k is the Boltzmann constant, and T is the temperature. Perez et. al. calculated the sintering time for tin oxide and gold nanoparticles using the finite element simulation method [47]. The sintering of gold (0.061 ms) was much faster than that of tin oxide (2.755 ms), which is inversely proportional to the surface diffusivity and surface energy, as expressed in Equation (3). Because the stable tin oxide layer is covered with as-synthesized Sn NP surfaces (Fig. 3d), the curing

time required for fully grown Sn NPs takes hours (Fig. 4c). Another factor affecting the grain growth of Sn NPs is the existence of the substrate (*h*-BN) on which Sn NPs were decorated. Tsai et al. [48] performed classical MD simulations to compare the coalescence and melting behaviors of two copper nanoparticles (Cu NPs) in the absence and presence of a graphene substrate. The results showed that the coalescence and melting temperatures are both sensitive to the particle size and the presence of the substrate. From the simulation results obtained by Tsai [48], it could be reasonably postulated that the van der Waal interactions between the *h*-BN substrate and Sn NPs inhibit the coalescence of Sn NPs. Thus, Sn NPs impregnated on the *h*-BN surfaces have a relatively higher onset temperature of coalescence than isolated NPs. Because of the Sn oxide layer and *h*-BN substrate effect, the optimized curing time required for the highest thermal conductivity induced by Sn NP coalescence was 60 min, which is much longer than expected to isolate tin nanoparticles (Fig. 4c).

Since the number of conductive pathways or networks formed by the thermally conductive filler determines the thermal conductivity of the composite, the dispersion state of the filler and inter particle bonding in the polymer matrix are strongly related to the thermal conductivity. Fig. 5 shows the SEM micrographs of the cured epoxy composites. As shown in Fig. 5a-e, the procedure of Sn NP growth is indicated from as-synthesized Sn NPs to Sn NPs on *h*-BN-filled epoxy polymer composites with respect to the final curing temperature at 50 wt. % filler loading. The average size of the Sn NPs is approximately 100 nm (Fig. 5a), and its shape becomes circular in the cured composite with increasing curing temperature; moreover, the average size increases based on the maximum size: ~500 nm at 180 ℃, ~1 μm at 200 ℃, and over 1 μm at 220–240 ℃. As the temperature gets close to above the Sn melting point (231℃), the fully grown Sn NPs by coalescence were completely melted and exhibited a circular shape, representing non-wetting behavior against the *h*-BN surfaces (Fig. 5e). Fig. 5f shows the SEM image of the maximum amount of filler loading at 68 wt. %. Moreover, the thermally percolated *h*-BN fillers via Sn NP coalescence were quite effective in increasing the thermal conductivity

of high Sn NPs on *h*-BN-loaded epoxy composites without any external forces. The sintered Sn micron-size particles connect the h-BN fillers with each other without epoxy resin at the interface between Sn NPs and *h*-BN in the epoxy matrix (Fig. 6 a-d), implying that the interface phonon scattering is reduced by phonon frequency mismatch because of the epoxy layer between the *h*-BN fillers.

3.3. Dielectric Properties and Thermal Expansion Coefficients

Fig. 7a and b shows the dielectric constant and loss of the hybrid-filler-embedded epoxy with respect to the amount of hybrid filler. The dielectric constant of the hybrid-filler-embedded epoxy increases with the amount of hybrid filler but reaches a plateau at 8. Notably, the composites do not exhibit dielectric dispersion at low frequencies below 1 MHz. The dielectric loss of the composite is also insensitive to the addition of the hybrid filler. This indicates that tin metal particles do not form a tin network through melting or wetting on *h*-BN. The SEM micrograph of Sn NPs on *h*-BN-filled epoxy composite shows discrete and spherical nanoparticles dispersed in the epoxy matrix (Fig. 5e-f). The wetting behavior of melted tin could be explained via a contact angle of three phase relationships [49]: $\gamma_{BE} = \gamma_{BS} + \gamma_{SE} \cos\theta$ i.e., $\cos\theta = (\gamma_{BE} - \gamma_{BS})/\gamma_{SE}$, where γ_{BE}, γ_{BS}, and γ_{SE} are the interface energies of *h*-BN/epoxy, *h*-BN/Sn, and Sn/epoxy, respectively. A low-contact angle makes the tin liquid to spread over the *h*-BN filler, providing a possibility of continuous tin phase that might increase the electrical conductivity of the composite. On the other hand, a high-contact angle indicates poor wetting; hence, the tin liquid shrinks from the *h*-BN solid. The measured contact angle and value of cos θ were ~145° and −0.819, respectively, as shown in Fig. 5e. The negative sign of cos θ indicates that the interface energy of *h*-BN/epoxy was lower than that of *h*-BN/Sn ($\gamma_{BE} \leq \gamma_{BS}$), implying the *h*-BN/Sn interface tried to be minimize compared with *h*-BN/epoxy interface to stabilize the total energy of the epoxy composite. It is concluded that the non-wetting behavior of the sintered Sn NPs on the h-BN surfaces gives rise to a low dielectric constant and loss (Fig. 7a

and b), indicating that the entire composite could maintain electrical insulation. In semiconductor packaging materials, not only a high thermal conductivity but also a low expansion coefficient plays an important role in the reliability of electronic devices. The CTE of hexagonal boron nitride is −2.7 ppm °C $^{-1}$ for the in-plane direction and 38 ppm °C $^{-1}$ for the out-of-plane direction owing to the anisotropic property of the lattice structure *h*-BN. In Fig. 7c-d, the linear dimensional change and CTE of Sn NPs on *h*-BN epoxy composites were measured at a temperature range of 20–150 ℃. The CTE of pure epoxy (65 ppm °C $^{-1}$) was so high that the addition of 60 wt. % *h*-BN could reduce the CTE to 32 ppm °C $^{-1}$. The randomly distributed *h*-BN fillers and negative in-plane CTE of *h*-BN could be attributed to the CTE reduction of the composites. The CTE of Sn NPs on *h*-BN-loaded epoxy composite was in the range of 37~34 ppm °C $^{-1}$ at a loading range of 65~68 wt. %. There is no significant difference in the CTE of the epoxy composite regardless of whether the Sn metal nanoparticles presented on the *h*-BN surfaces; this can be attributed to the slightly low CTE (23.4 ppm °C^{-1}) of Sn compared with the out-of-plane CTE of *h*-BN (⊥ 38 ppm °C^{-1}).

4. Conclusions

A newly developed thermally conductive epoxy composite incorporated with hexagonal boron nitride (*h*-BN) decorated with tin nanoparticles (Sn NPs) was fabricated to investigate its applicability in electronic device packaging. Hybrid fillers (Sn NPs on *h*-BN) were successfully synthesized by $NaBH_4$-mediated reduction reaction, where the particle size, shape, and homogeneity were completely controlled by the NMP/EtOH co-solvent ratios. With increasing NMP proportion, the size distribution of Sn NPs was more uniform, and their sizes were much smaller than those obtained when employing EtOH as the solvent. The highest thermal conductivity of the epoxy composite was found to be 11.9 W m^{-1} K^{-1} at 68 wt. % loading without any external force. The high thermal conductivity can be mainly attributed to the

thermal diffusivity brought on by the improvement in the thermally conductive 3D network of the hybrid fillers (Sn NPs on *h*-BN) in the epoxy resin by in situ growth of Sn NPs having low melting temperature during the curing process. The temperature and time required for fully grown Sn NPs to exhibit a sufficient size to interconnect *h*-BN were optimized to be 240 ℃ and 60 min, respectively; the thermal conductivity was more sensitive to the curing temperature than the curing time. The coalescence of Sn NPs was inhibited by both the stable tin oxide layer and the van der Waals interaction with Sn NPs and *h*-BN substrate, inducing a relatively higher onset temperature for coalescence and a much longer time than expected to isolate the tin nanoparticles. The dielectric constant (D_k) and loss (D_f) of the 68 wt. % hybrid-filler-embedded epoxy resin were measured to be 7.52 and 0.023 at 1 MHz, respectively. This indicates that the entire composite could maintain electrical insulation owing to the non-wetting behavior of the sintered Sn NPs on the h-BN surfaces. The CTE of Sn NPs on the *h*-BN-loaded epoxy composite was in the range of 37~34 ppm $°C^{-1}$ at a loading rate range of 65~68 wt. %. There was no significant difference in the CTE of the epoxy composite regardless of whether the Sn metal nanoparticles presented on the *h*-BN surfaces. Epoxy composites prepared using thermally conductive Sn NPs on *h*-BN hybrid fillers exhibiting low dielectric values (D_k and D_f) and relatively low CTE are expected to be promising candidates for next-generation electronic packaging industry.

Credit authorship contribution statement

Lee E. S: Conceptualization and Data curation, Investigation, Formal analysis, writing original draft, Writing - review & editing, Supervision. **Kang J. G & Kang M. K:** Investigation, Formal analysis. **Kim K. H:** Formal analysis. **Park S. T:** Formal analysis. **Kim Y. S:** Formal analysis. **Kim I:** Project administration. **Kim S. D.:** Project administration. **Bae J. Y:** Writing original draft & editing.

Declaration of competing interest

The authors declare that they have no known competing financial interests or personal relationships that could have appeared to influence the work reported in this paper.

Acknowledgements

We would like to thank Prof. Lee J-C (Department of Materials Science and Engineering, Sungkyunkwan University) for his help with the dielectric measurements of the epoxy composites. We also thank Baek W. J. (SAIT) for TEM measurement and mapping analysis.

This research did not receive any specific grant from funding agencies in the public, commercial, or not-for-profit sectors.

Appendix A. Data availability Statement

The datasets generated and/or analyzed during this study can be made available from the corresponding author on reasonable request.

References

[1] Tummala RR, Rymaszewski EJ. Microelectronic Packaging Handbook. Van Nostrand Reinhold, New York, 1989;523-658.

[2] Kim W, Bae J-W, Choi I-D, Kim Y-S. Thermally conductive EMC (epoxy molding compound) for microelectronic encapsulation. Polym Eng Sci 1999;39(4):756-766.

[3] Lide DR. Handbook of Physics and Chemistry. CRC Press: Boca Raton, 1999;12-200–201,12-97–107.

[4] Bujard P, Kuhnlein G, Ino S, Shiobara T. Thermal conductivity of molding compounds for plastic packaging. IEEE Trans Comp Pack Manu Technol Part A 1994;17(4):527-532.

[5] Huang X, Jiang P, Tanaka T. A review of dielectric polymer composites with high thermal conductivity. IEEE Electrical Insulation Magazine 2011;27(4):8-16.

[6] Hong H, Kim J-U, Kim T-I. Effective assembly of nano-ceramic materials for high and anisotropic thermal conductivity in a polymer composite. Polymers 2017;9(9):413.

[7] Weng Q, Wang X, Bando Y, Golberg D. Functionalized hexagonal boron nitride nanomaterials: emerging properties and applications. Chem Soc Rev 2016;45:3989-4012.

[8] Nan CW, Birringer R, Clarke DR, Gleiter H. Effective thermal conductivity of particulate composites with interfacial thermal resistance. J Appl Phys 1997;81(10):6692.

[9] Yu C, Zhang J, Li Z, Tian W, Wang L, Luo J, Li Q, Fan X, Yao Y. Enhanced through-plane thermal conductivity of boron nitride/epoxy composites. Composites: Part A 2017; 98:25-31.

[10] Han J, Du G, Gao W, Bai H. An anisotropically high thermal conductive boron nitride/epoxy composite based on nacre-mimetic 3D network. Adv Funct Mater 2019; 29:1900412.

[11] Kargar F, Barani Z, Salgado R, Debnath B, Lewis JS, Aytan E, Lake RK., Balandin AA. Thermal percolation threshold and thermal properties of composites with high loading of graphene and boron nitride fillers. ACS Appl Mater Interfaces 2018;10(43):37555-37565.

[12] Lewis JS, Barani Z, Magana AS, Kargar F, Balandin AA. Thermal and electrical conductivity control in hybrid composites with graphene and boron nitride fillers. Mater Res Express 2019;6(8):085325.

[13] Lewis JS, Perrier T, Barani Z, Kargar F, Balandin AA. Thermal interface materials with graphene fillers: review of the state of the art and outlook for future applications. Nanotechnology 2021;32(14):142003.

[14] Fu Y, Hansson J, Liu Y, Chen S, Zehri A, Samani MK, Wang N, Ni Y, Zhang Y, Zhang Z-B, Wang Q, Li M, Lu H, Sledzinska M, Torres CMS, Volz S, Balandin AA, Xu X, Liu J. Graphene related materials for thermal management. 2D Mater 2020;7(1):012001.

[15] Wang Z, Meng L, Wang L, Tian L, Chen S, Wu G, Kong B, Cheng Y. Simultaneously enhanced dielectric properties and through-plane thermal conductivity of epoxy composites with alumina and boron nitride nanosheets. Sci Rep 2021; 11:2495.

[16] Lee E-S, Lee S-M, Shanefield DJ, Cannon WR. Enhanced thermal conductivity of polymer matrix composite via high solids loading of aluminum nitride in epoxy resin. J Am Ceram Soc 2008;91(4):1169-74.

[17] Chen H, Ginzburg V, Yang J, Yang Y, Liu W, Huang Y, Du L, Chen B. Thermal conductivity of polymer-based composites: Fundamentals and applications. Prog Polym Sci 2016; 59:41-85.

[18] Hu J, Huang Y, Yao Y, Pan G, Sun J, Zeng X, Sun R, Xu JB, Song B, Wong CP. Polymer Composite with Improved Thermal Conductivity by Constructing a

Hierarchically Ordered Three-Dimensional Interconnected Network of BN. ACS Appl Mater Interfaces 2017;9:13544-53.

[19] Burger N, Laachachi A, Ferriol M, Lutz M, Toniazzo VR. Review of thermal conductivity in composites: Mechanisms, parameters and theory. Prog Polym Sci 2016; 1:1-28.

[20] Wu K, Liao P, Du R-N, Zhang Q, Chen F, Fu Q, Preparation of a thermally conductive biodegradable cellulose nanofiber/hydroxylated boron nitride nanosheet film: the critical role of edge-hydroxylation. J Mater Chem A 2018; 6:11863-73.

[21] Yang J, Li X-F, Han S, Yang R-Z, Min P, Yu Z-Z. High-quality graphene aerogels for thermally conductive phase change composites with excellent shape stability. J Mater Chem A 2018; 6:5880-86.

[22] Xu Y, Yang C, Li J, Mao X, Zhang H, Hu S, Wang S. Development of AlN/Epoxy Composites with Enhanced Thermal Conductivity. Mater 2017; 10:1442.

[23] Hu Y, Du G, Chen N, A novel approach for Al_2O_3/epoxy composites with high strength and thermal conductivity. Comp Sci Technol 2016; 124:36-43.

[24] Hao LC, Li ZX, Sun F, Ding K, Zhou XN, Song ZX, Shi ZQ, Yang JF, Wang B. High-performance epoxy composites reinforced with three-dimensional Al_2O_3 ceramic framework. Composites Part A 2019; 127:105648.

[25] Yu J, Mo H, Jiang P. Polymer/boron nitride nanosheet composite with high thermal conductivity and sufficient dielectric strength. Polym Adv Technol 2015; 26:514-520.

[26] Wang F, Yao Y, Zeng X, Huang T, Sun R, Xud J, Wong CP. Highly thermally conductive polymer nanocomposites based on boron nitride nanosheets decorated with silver nanoparticles. RSC Adv 2016; 6:41630-36.

[27] Huang T, Yao Y, Zhang G, Meng F. Silver Nanoparticle-Deposited Aluminum Oxide Nanoparticle as Fillers for Epoxy Composites with High Thermal Conductivity. Adv Comp Lett 2018;27(6):245-250.

[28] Liu Z, Li J, Liu X. Novel Functionalized BN Nanosheets/Epoxy Composites with Advanced Thermal Conductivity and Mechanical Properties. ACS Appl Mater Interfaces, 2020;12:6503–6515.

[29] Chen L, Xiao C, Tang Y, Zhang X, Zheng K, Tian X. Preparation and characterization of epoxy-based composite with multilayered structure and high thermal conductivity. Mater Res Express 2019; 6:075314.

[30] Xiao C, Tang Y, Chen L, Zhang X, Zheng K, Tian X. Preparation of highly thermally conductive epoxy resin composites via hollow boron nitride microbeads with segregated structure. Composites Part A 2019; 121:330-340.

[31] Zhang T, Sun J, Ren L, Yao Y, Wang M, Zeng X, Sun R, Xu J-B, Wong C-P. Nacre-inspired polymer composites with high thermal conductivity and enhanced mechanical strength. Composites Part A 2019; 121:92-99.

[32] Chen C, Xue Y, Li Z, Wen Y, Li X, Wu F, Li X, Shi D, Xue Z, Xie X. Construction of 3D boron nitride nanosheets/silver networks in epoxy-based composites with high thermal conductivity via in-situ sintering of silver nanoparticles. Chem Eng J 2019; 369:1150-60.

[33] Temgire MK, Joshi SS, Radiat MR, Yadav AA. Optical and structural studies of silver nanoparticles. Phys Chem 2004; 71:1039-1044.

[34] Darroudi M, Mansor BA, Kamyar S, Abdul AH, Nor AI. Synthesis and characterization of UV-irradiated silver/montmorillonite nanocomposites. Solid State Sci 2009; 11:1621-24.

[35] Foroozmehr E, Alemohammad H, Wang X, Toyserkani E, Esmaeili S. Laser-assisted surface patterning of magnesium with silver nanoparticles: synthesis, characterization and modelling. J Phys D: Appl Phys 2011; 44:495305.

[36] P-Santos I, L-Marzán LM. Reduction of silver nanoparticles in DMF. Formation of monolayers and stable colloids. Pure Appl Chem 2000; 72:83-90.

[37] Kim I-T, Lee J, An J-C, Jung E, Lee H-K, Morita M, Shim J. Capacity Improvement of Tin-Deposited on Carbon-Coated Graphite Anode for Rechargeable Lithium Ion Batteries. Int J Electrochem Sci 2016; 11:5807-18.

[38] Torigoe K, Nakajima Y, Esumi K. Preparation and Characterization of Colloidal Silver-Platinum Alloys. J Phys Chem 1993; 97:8304-09.

[39] Reichardt C, Welton T. Solvent and Solvent Effects in Organic Chemistry: WILEY-VCH Verlag GmbH & Co. Weinheim, 2003;255.

[40] Howard H, Eliel EL. Reductions with Metal Hydrides. X. The Stereochemistry of Reduction of 3,3,5-Trimethylcyclohexanone with Complex Aluminohydrides. J Am Chem Soc 1962; 84:2363-68.

[41] Torisawa Y, Nishi T, Minamikawa JI. $NaBH_4$ in N-Methylpyrrolidone: A Safe Alternative for Hydride Displacement Reaction. Bioorg Med Chem Lett 2001; 11:2787–2789.

[42] Brown HC, Mead EJ, Rao BCS. A Study of Solvents for Sodium Borohydride and the Effect of Solvent and the Metal Ion on Borohydride Reductions. Organic Biol Chem 1955; 77:6209-13.

[43] Coblenz WS, Dynys JM, Cannon RM, Coble RL. Initial stage solid state sintering models. A critical analysis and assessment. Mater Sci Res 1980; 13:141-157.

[44] Kuczynski GC. Self-Diffusion in Sintering of Metallic Particles. Trans Metall Soc AIME 1949; 85:169-78.

[45] Kuczynski GC. The mechanism of densification during sintering of metallic particles. Acta Metall 1956;4(1):58–61.

[46] M. N. Rahaman, *Ceramic Processing and Sintering*, Marcel Dekker, Inc. **1995**, Chap. 8, 398.

[47] Perez C, Walton S, Wiswall J, Bakrania S. Simulating tin dioxide and gold nanoparticle sintering using finite element method. MECHENG 599-03 Final Project: Class website: www-personal.engin.umich.edu/ ~weilu/ teaching/ teaching.html, 2005.

[48] Tsai P-C, Jeng Y-R. Coalescence and epitaxial self-assembly of Cu nanoparticles on graphene surface: A molecular dynamics study. Comput Mater Sci 2019; 156:104-110.

[49] German RM, Suri P, Park S-J. Review: liquid phase sintering. J Mater Sci 2009; 44:1.

Figures

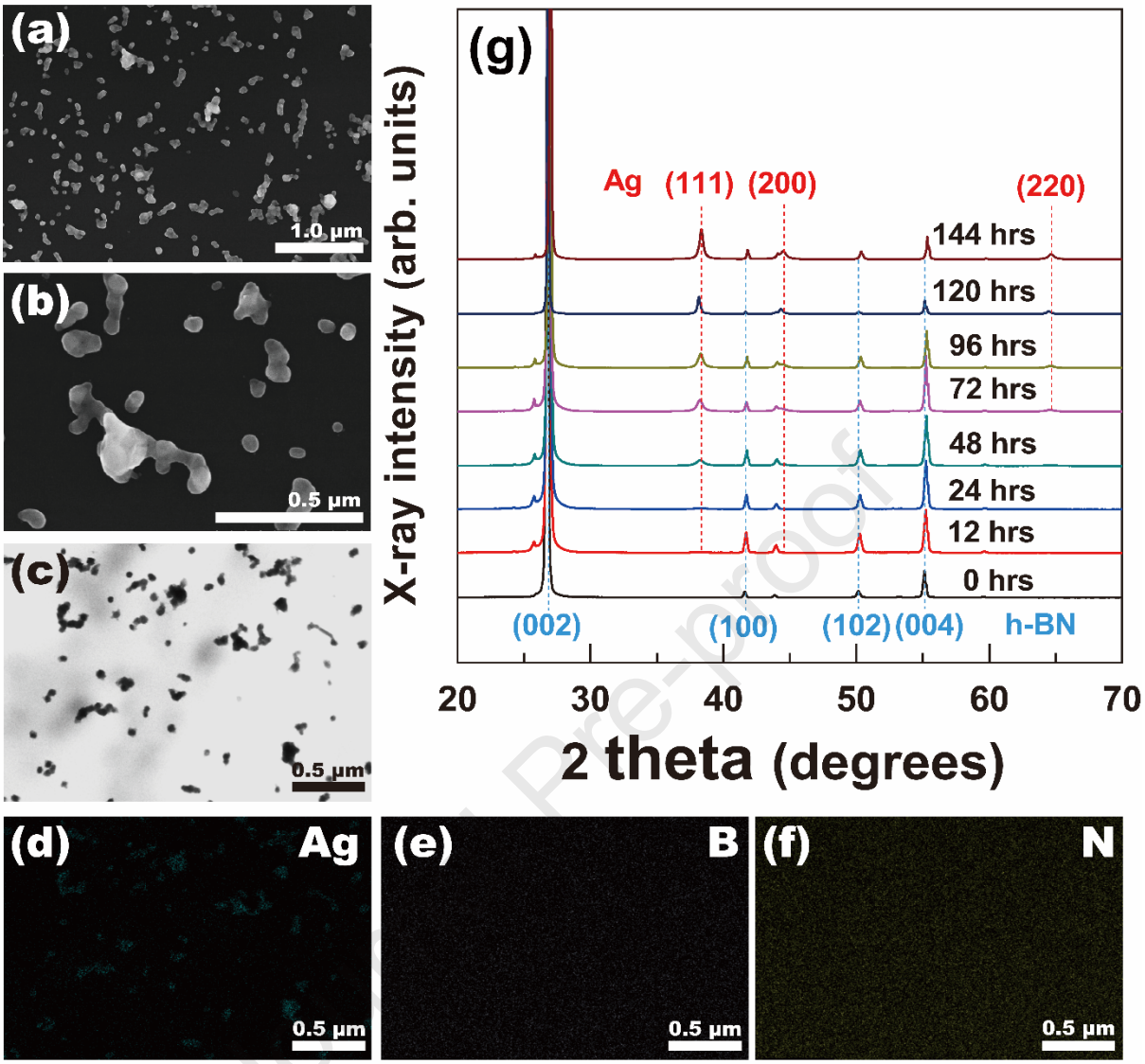

Fig. 1. Microstructure and EDS analysis of Ag NPs formed on *h*-BN (boron nitride) surfaces following a 144 h reaction: (a)-(b) SEM micrographs of Ag NPs on *h*-BN with high and low magnifications, (c) high-angle annular dark field-scanning electron microscope (HAADF-SEM) image of Ag NPs on *h*-BN. Corresponding EDS elemental mappings of (d) silver, (e) boron, and (f) nitrogen. (g) XRD patterns of Ag NPs formed on *h*-BN (boron nitride) surfaces with respect to the reaction time from unreacted to 144 h. The ratio of $AgNO_3$: *h*-BN powder is 1:1 wt. % in the DMF (80 mL) solvent.

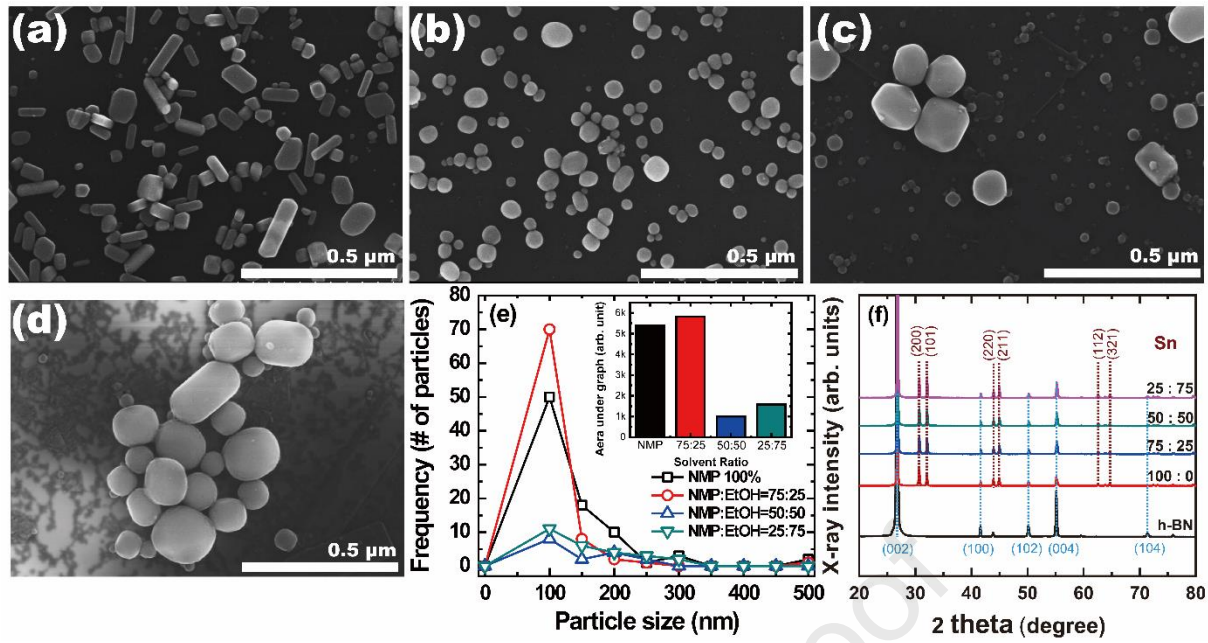

Fig. 2. SEM micrographs and XRD patterns of Sn NPs formed on h-BN (boron nitride) surfaces corresponding to *h*-BN: $SnCl_4 \cdot 5H_2O$ ratios of 1:1.5 wt.% under NMP: EtOH solvent ratio of: (a) 100:0, (b) 75:25, (c) 50:50, and (d) 25:75; (e) particle size analysis with image pro® plus software with respect to the changes in the solvent ratio. The area under the graphs is shown in the inset to demonstrate the amount of synthesized Sn NPs. (f) XRD patterns of Sn NPs formed on *h*-BN (boron nitride) surfaces with respect to NMP: EtOH solvent ratios ranging from 100:0 to 25:75.

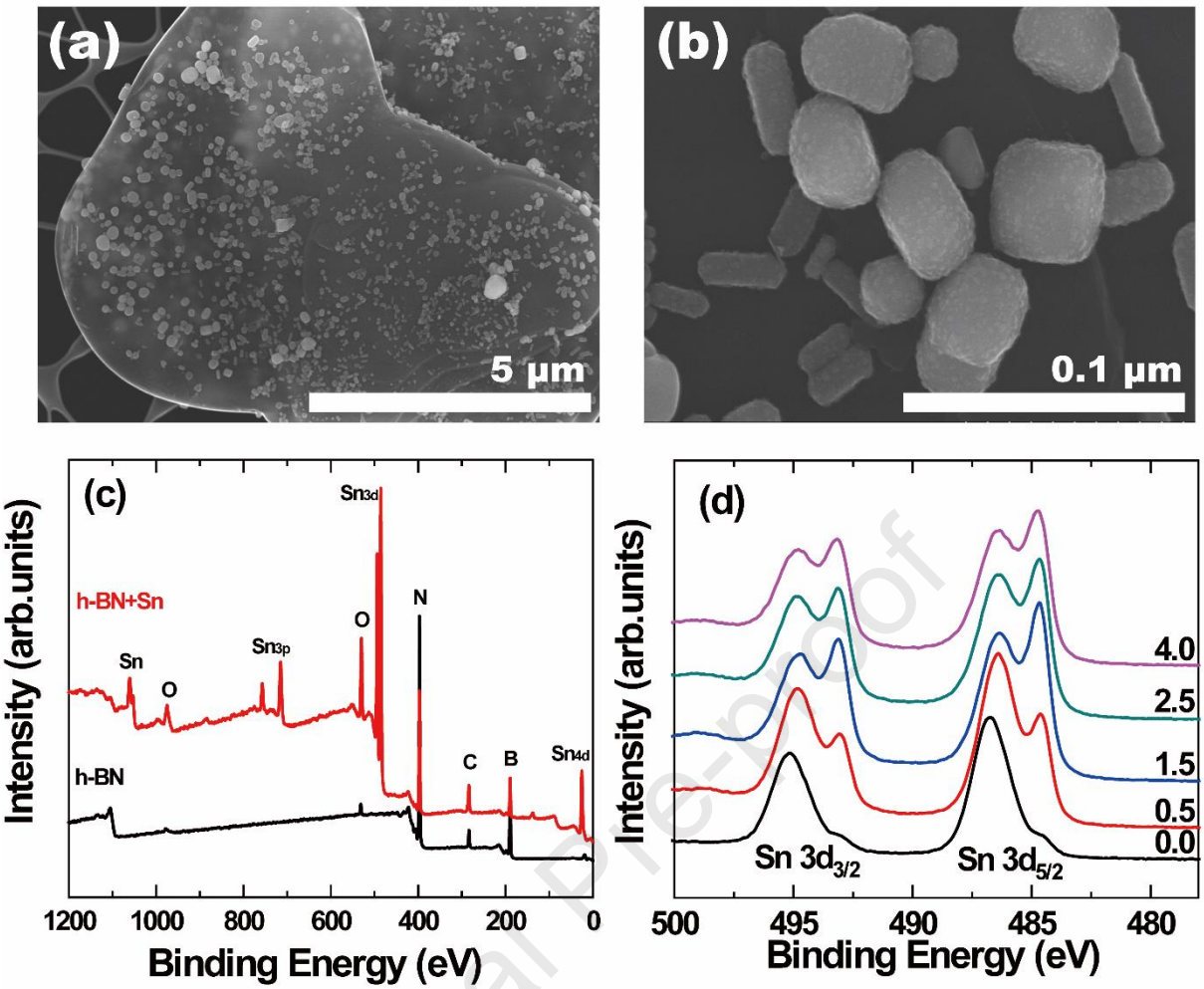

Fig. 3. SEM images and X-ray photoelectron spectrometry (XPS) analysis of Sn NPs formed on *h*-BN (boron nitride) surfaces at 1:2.5 wt.% ratio of *h*-BN: $SnCl_4 \cdot 5H_2O$ in 100% NMP solution: (a)-(b) SEM micrographs of Sn NPs on *h*-BN with high and low magnifications, (c) XPS results of Sn NPs on *h*-BN and pure *h*-BN with survey scans, (d) XPS results of Sn NPs on *h*-BN showing Sn 3d spectra with respect to various Ar-ion beam sputtering times: 0.0, 0.5, 1.5, 2.5, and 4.0 min.

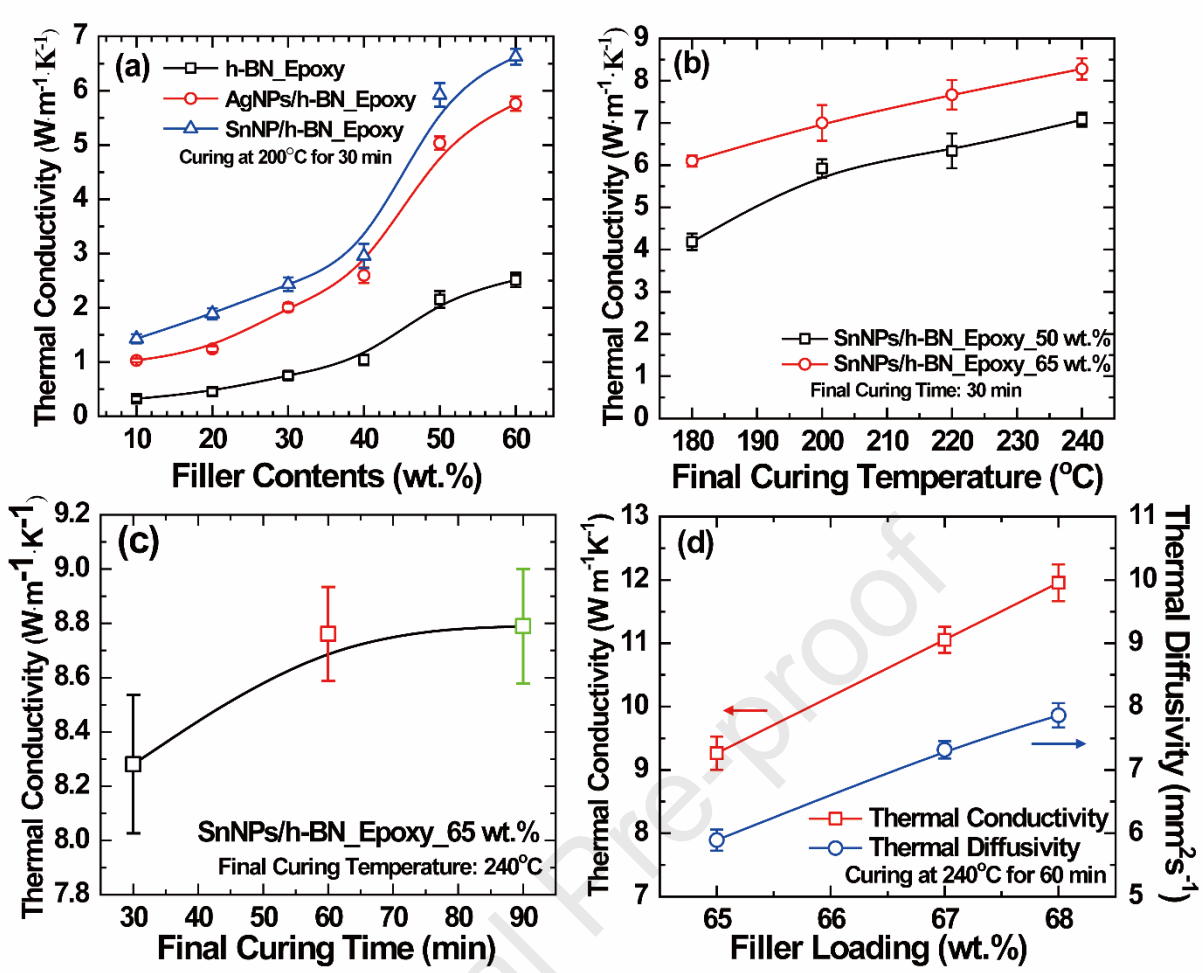

Fig. 4. Thermal conductivity of hybrid metal filler-loaded epoxy composites: (a) with respect to the three types of fillers, i.e., *h*-BN, Ag NPs on *h*-BN, and Sn NPs on *h*-BN filler loading in the low filler loading region (< 60 wt.%), (b) thermal conductivity changes of Sn NPs on *h*-BN-filled composites with respect to the final curing temperature, (c) final curing time, (d) thermal conductivity and diffusivity changes of Sn NPs on *h*-BN-filled epoxy composites in the high filler loading region (> 65 wt.%).

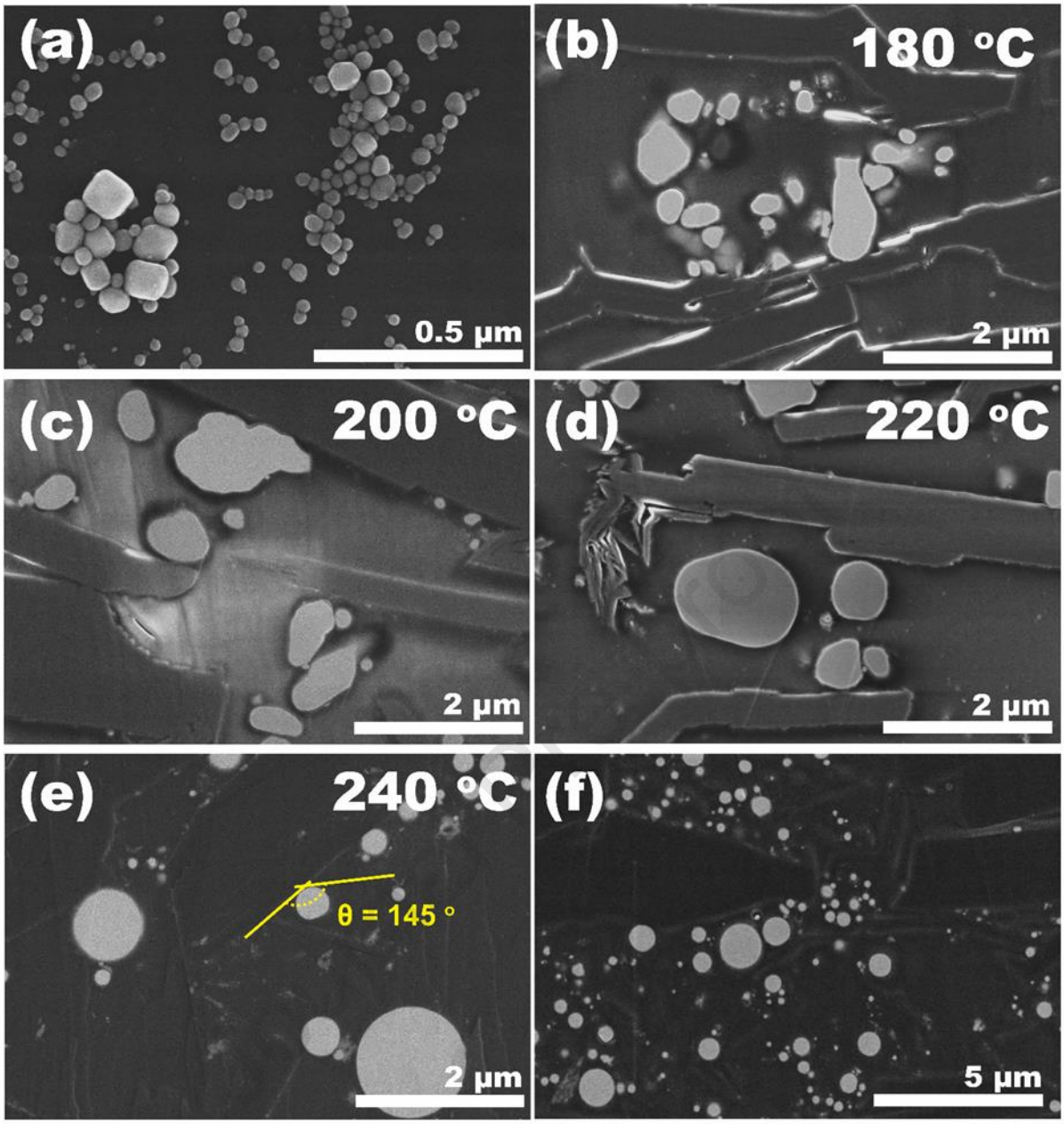

Fig. 5. SEM micrographs of Sn NPs on *h*-BN surfaces and cross-sectional SEM images of hybrid filler-loaded epoxy composite: (a) SEM images of Sn NPs on *h*-BN at 1:1.5 wt.% ratio of *h*-BN: $SnCl_4 \cdot 5H_2O$ in 25:75 EtOH: NMP solution. (b)-(e) Cross sectional view of Sn NPs on *h*-BN powder-filled epoxy polymer composites with respect to the final curing temperature at 50 wt.% filler loading: (b) 180 ℃, (c) 200 ℃, (d) 220 ℃, and (e) 240 ℃; (f) high Sn NPs on *h*-BN loading of epoxy composite at 68 wt.% under curing at 240 ℃ for 60 min.

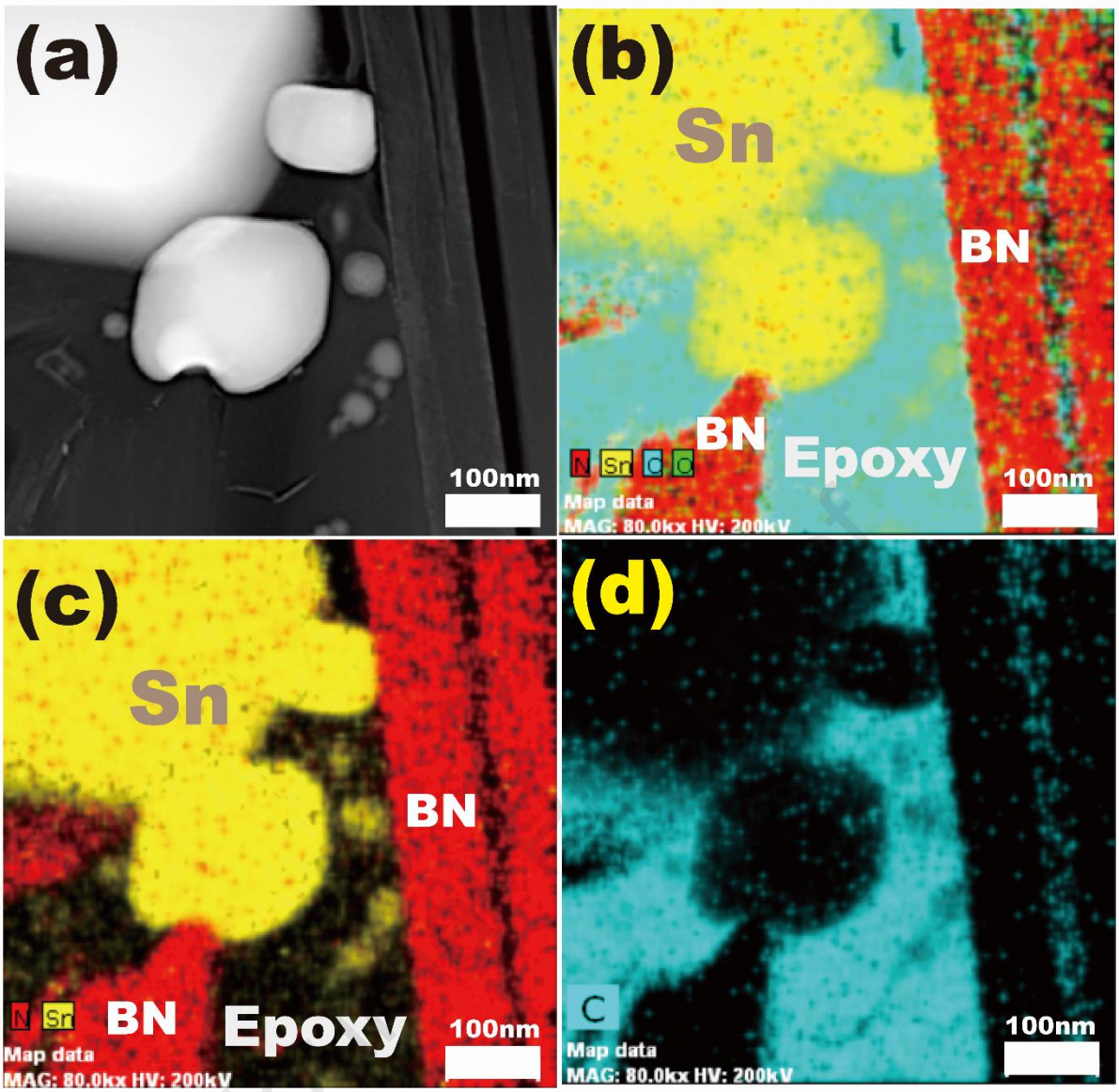

Fig. 6. TEM micrographs and corresponding EDS elemental mappings of Sn NPs on *h*-BN (boron nitride)-filled epoxy composites: (a) high-angle annular dark field-scanning electron microscope (HAADF-SEM) image of Sn NPs on *h*-BN-filled epoxy composites. (b)-(d) corresponding EDS mapping of (b) total elements, (c) Sn and BN, and (d) Carbon element only.

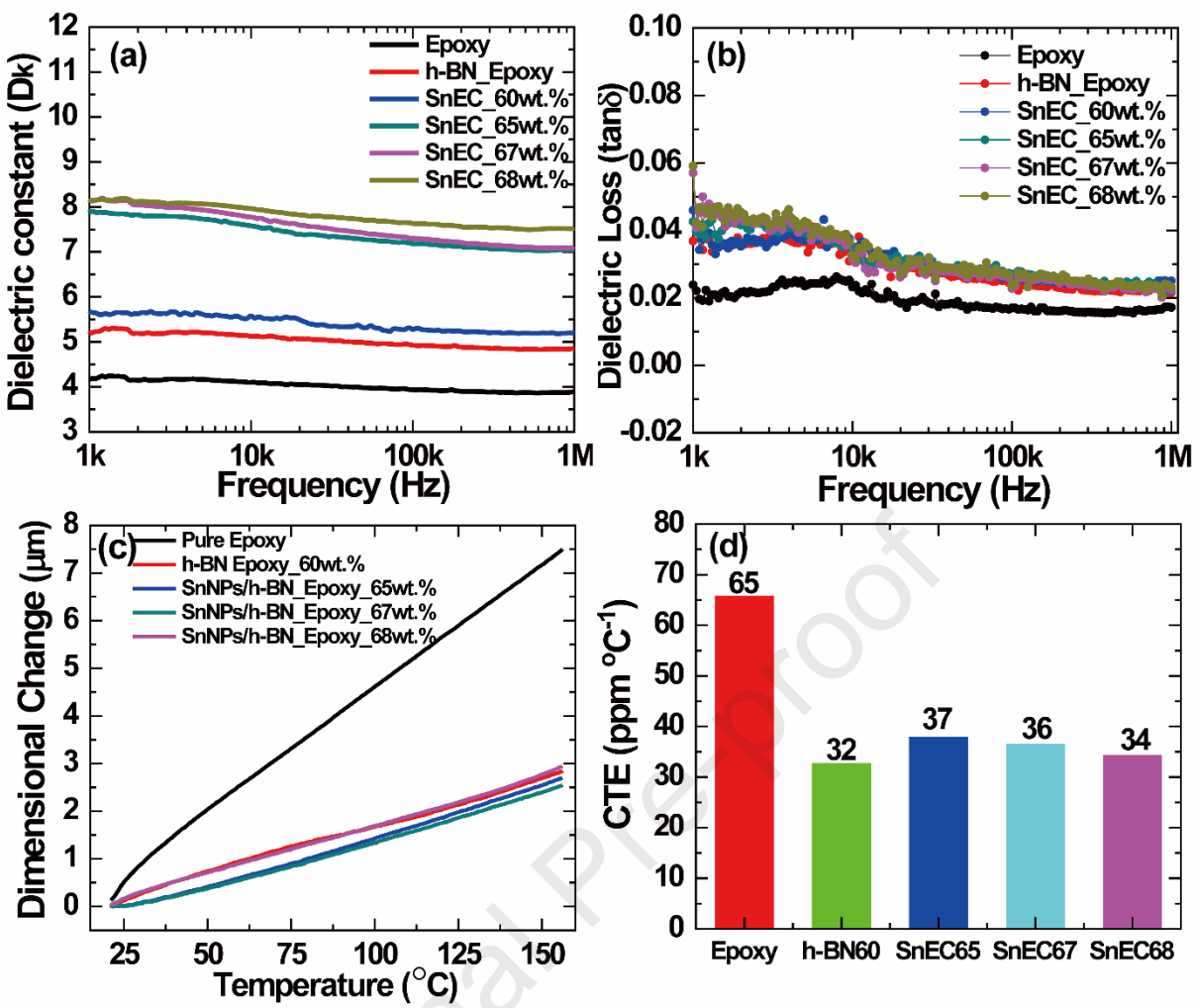

Fig. 7. Dielectric properties and linear dimensional changes of Sn NPs on *h*-BN-filled epoxy composites (SnEC) with respect to different volume fractions: (a) dielectric constant; (b) tan delta. (c) dimensional changes, and (d) coefficient of thermal expansion (CTE) of epoxy resin, and *h*-BN, Sn NPs on *h*-BN-loaded epoxy composites (SnEC) with various filler loading.

Supporting Information

High Thermal Conductivity of Boron Nitride-Filled Epoxy Composites Prepared by Tin Solder Nanoparticle Decoration

Eun-Sung Lee, Jong-Gu Kang, Min-Kyeong Kang, Ki-Hong Kim, Seon-Tae Park, Yong Su Kim, In Kim, Sung-Dug Kim, and Jin-Young Bae**

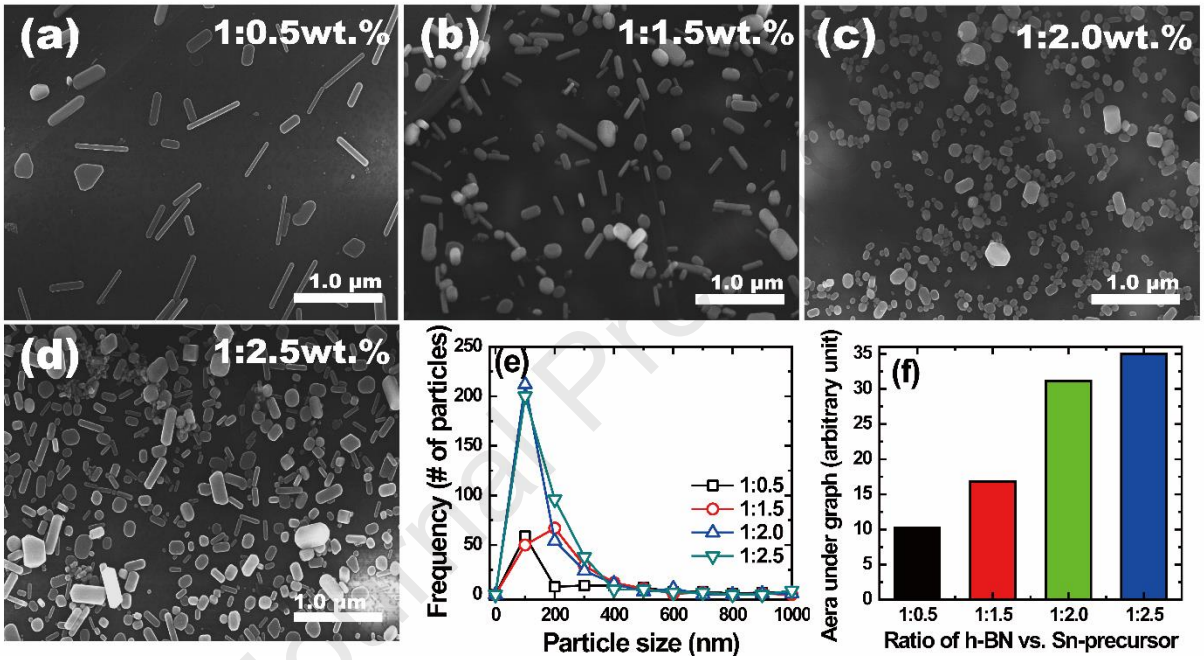

Supplementary Fig. S1. SEM micrographs of Sn NPs formed on *h*-BN (boron nitride) with respect to the wt.% ratio of h-BN vs. $SnCl_4 \cdot 5H_2O$: (a) 1:0.55, (b) 1:1.5, (c) 1:2, and (d) 1:2.5; (e)-(f) particle size analysis with image pro® plus software.

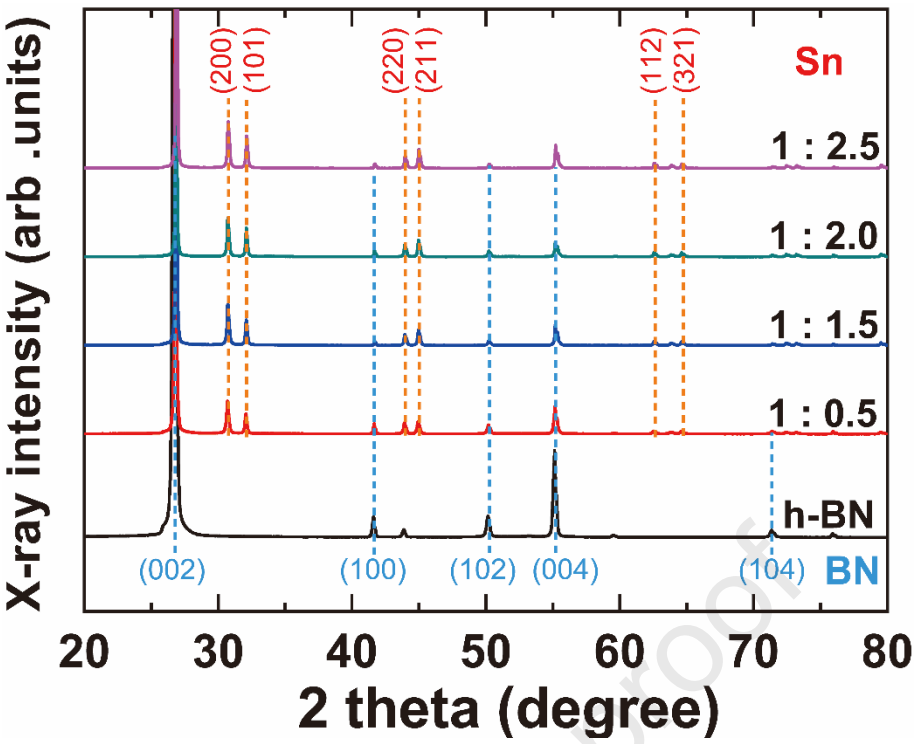

Supplementary Fig. S2. XRD patterns of Sn NPs formed on *h*-BN (boron nitride) with respect to increasing amount of *h*-BN vs. $SnCl_4 \cdot 5H_2O$ from 1: 0.5 to 1: 2.5 at 100% NMP solvent.

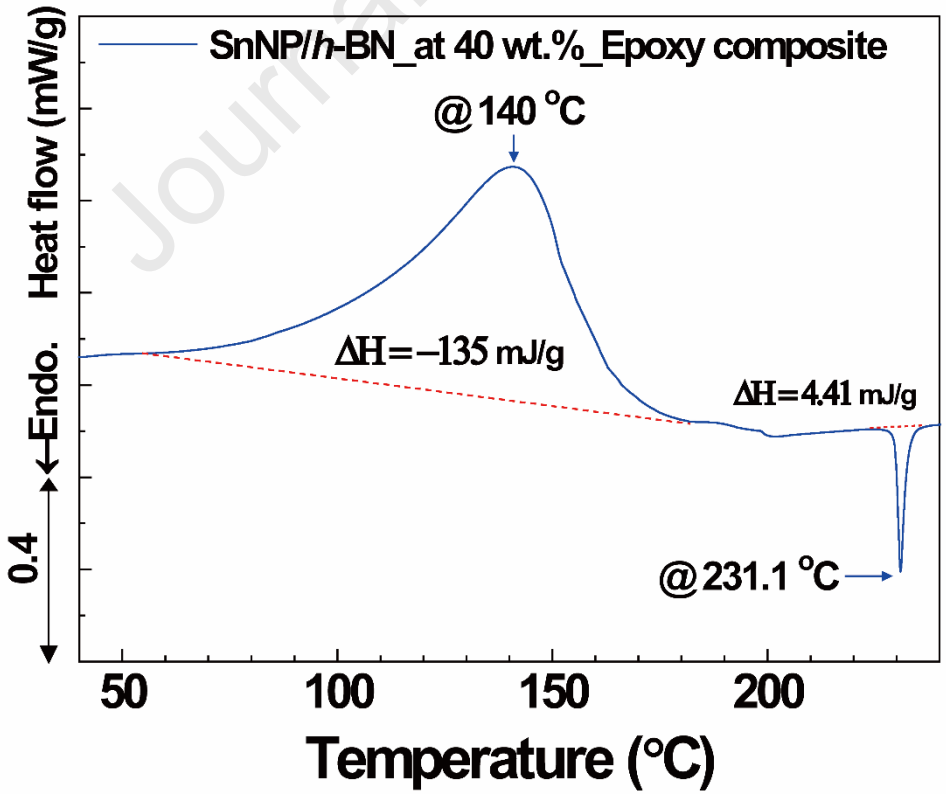

Supplementary Fig. S3. DSC curves of Sn NPs on *h*-BN (boron nitride)-filled epoxy composites at 40 wt. % loading. Ramping at 10 °C min^{-1} under N_2 atmosphere.

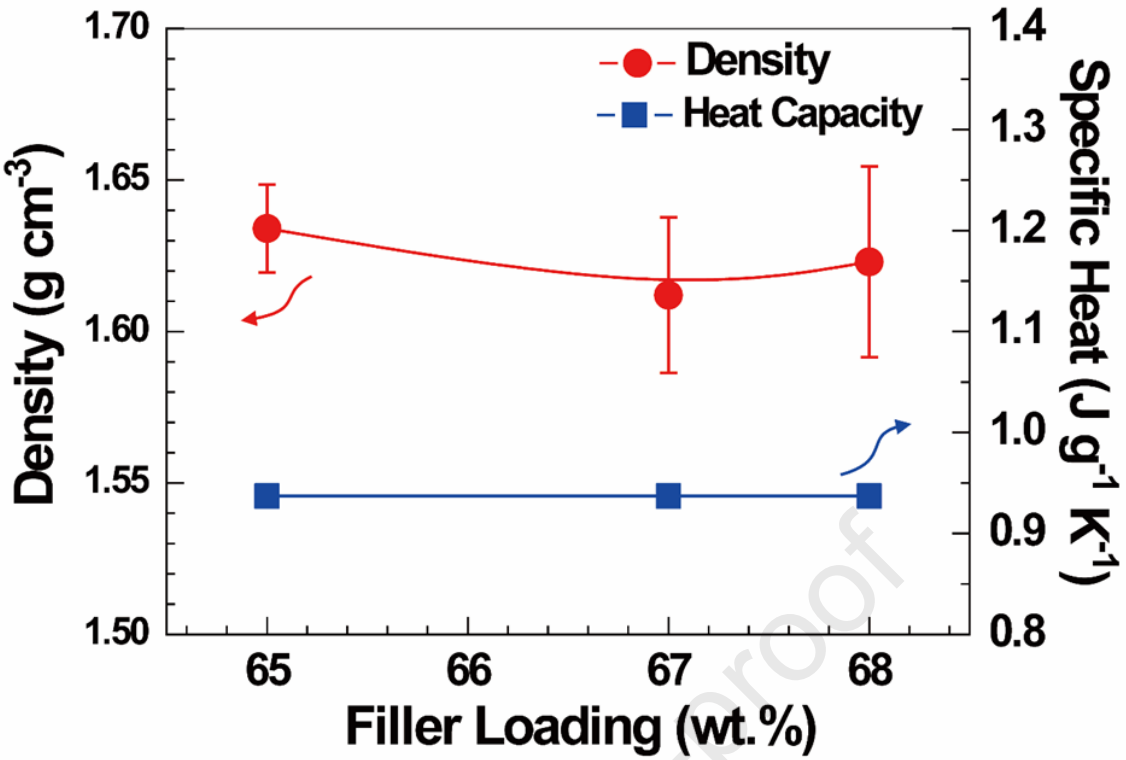

Supplementary Fig. S4. Bulk density and heat capacitance of Sn NPs on *h*-BN-filled epoxy composites with respect to the loading amount.

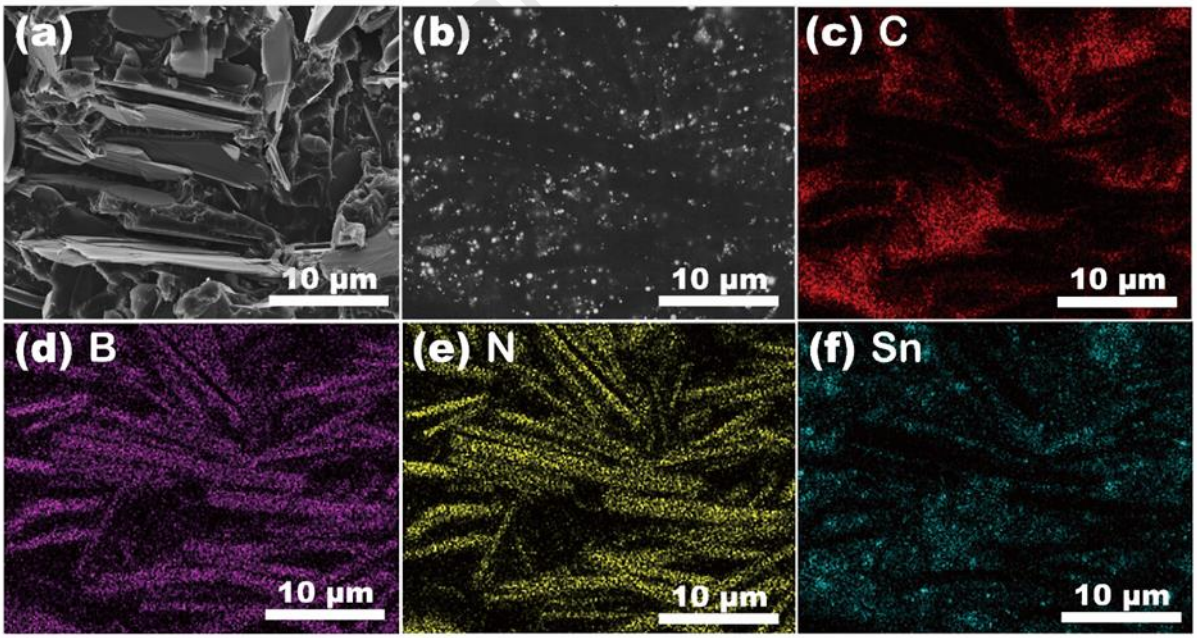

Supplementary Fig. S5. Cross-sectional SEM micrograph of Sn NPs on h-BN filled epoxy composite at 68 wt.% loading. (a) Fracture surface (b) Ion-milling surface: (c)-(f) EDS mapping images of epoxy composite, (c) Carbon, (d) Boron, (e) Nitrogen, (f) Tin, respectively, indicating a randomly distributed hexagonal boron nitride.

Declaration of competing interest

The authors declare that they have no known competing financial interests or personal relationships that could have appeared to influence the work reported in this paper.